Prospects for reconstructing the gravitational-wave signals from core-collapse supernovae with Advanced LIGO-Virgo and the BayesWave algorithm

Nayyer Raza,[1,2,*] Jess McIver,[1,†] Gergely Dálya,[3,4] and Peter Raffai[3]

[1]*Department of Physics and Astronomy, University of British Columbia, Vancouver, British Columbia V6T1Z1, Canada*
[2]*Department of Physics, McGill University, Montreal, Quebec H3A2T8, Canada*
[3]*Institute of Physics, Eötvös University, 1117 Budapest, Hungary*
[4]*Department of Physics and Astronomy, Universiteit Gent, B-9000 Gent, Belgium*

(Received 16 March 2022; accepted 17 August 2022; published 19 September 2022)

Our current understanding of the core-collapse supernova explosion mechanism is incomplete, with multiple viable models for how the initial shock wave might be energized enough to lead to a successful explosion. Detection of a gravitational-wave signal emitted in the initial few seconds after stellar core-collapse would provide unique and crucial insight into this process. With the Advanced LIGO and Advanced Virgo detectors expected to approach their design sensitivities soon, we could potentially detect this signal from a supernova within our galaxy. In anticipation of such a scenario, we study how well the BayesWave algorithm can recover the gravitational-wave signal from core-collapse supernova models in simulated advanced detector noise, and optimize its ability to accurately reconstruct the signal waveforms. We find that BayesWave can confidently reconstruct the signal from a range of supernova explosion models in Advanced LIGO-Virgo for network signal-to-noise ratios $\gtrsim 30$, reaching maximum reconstruction accuracies of $\sim 90\%$ at SNR ~ 100. For low SNR signals that are not confidently recovered, our optimization efforts result in gains in reconstruction accuracy of up to 20%–40%, with typical gains of $\sim 10\%$.

DOI: 10.1103/PhysRevD.106.063014

I. INTRODUCTION

Despite many detailed multiwavelength electromagnetic observations of core-collapse supernovae (CCSNe), the exact mechanism powering these explosions is not yet fully understood (see, e.g., Burrows and Vartanyan [1] and references therein). This is in part because the electromagnetic signal only escapes from the very outer layers of the star after shock break-out (SBO), on timescales of hours to days after the core collapses [2]. However, most of the critical explosion physics occurs in the very central core of the star within the first few seconds [3]. The thermodynamic state of the explosion in this crucial period is imprinted on to the escaping neutrino flux, which carries away almost all of the total explosion energy, $\sim 10^{53}$ ergs [4]. Nonspherical, accelerated mass motions in the dense supernova core at this time also produce gravitational waves (GWs), lasting $\lesssim 1$ s after core bounce, which then probe the internal dynamics of the explosion mechanism (see, e.g., Abdikamalov *et al.* [5] for a recent review). We can thus use multimessenger astronomy to study these highly energetic events and help solve the mystery of what powers CCSNe.

While Supernova SN1987A marked the first (and so far only) supernova for which the neutrino signal was also observed [6–8], GWs from CCSNe have not yet been detected [9,10]. This is especially challenging since CCSNe are rare events, expected to only occur approximately once or twice per century in large galaxies such as the Milky Way [11].

The Advanced LIGO [12] and Advanced Virgo [13] ground-based interferometric GW detectors are expected to achieve their design sensitivities for their fourth observing run [14]. At these sensitivities (along with the addition of new detectors such as KAGRA [15,16] and LIGO-India [17] in the future), we could potentially observe a Galactic CCSN with GWs [18,19]. In anticipation of such an event, in this study we follow up on the CCSN sensitivity analyzed in the all-sky short duration burst search of the most recent LIGO-Virgo observing run [10], and characterize how well the BayesWave algorithm [20] can reconstruct CCSN models embedded in Advanced LIGO and Advanced Virgo design sensitivity detector noise. We also aim to tune BayesWave for CCSN signals, and produce a set of recommendations to be used for analysis on a

*nayyer.raza@mail.mcgill.ca
†mciver@phas.ubc.ca

candidate detection that will optimize the reconstruction accuracy.

A. Core-collapse supernovae

CCSNe are the end stage of the life of massive stars with $M \gtrsim 8\ M_\odot$. When the mass of the central iron core exceeds the effective Chandrasekhar mass, runaway collapse of the core begins, marking the onset of the explosion. This value can vary between $M_{Ch} \sim 1.34$–$1.8\ M_\odot$, depending on a range of different properties of the progenitor star (see e.g., Woosley *et al.* [21] for a classic review). A shock forms between the supersonically infalling inner core of $\sim$0.6–0.8 $M_\odot$ and the subsonically infalling outer core of $\sim 0.6\ M_\odot$. As the temperature and density increases, the collapse is accelerated by photodissociation and electron capture, which also produces a burst of neutrinos that are initially trapped in the ultradense inner core. As the central density reaches nuclear density, the inner core cannot collapse any further and rebounds, transferring in-falling energy-momentum by launching a shock wave outwards.

This shock wave loses significant energy as it propagates through the still in-falling outer core and heats it, dissociating iron nuclei into free protons and neutrons. Furthermore, as the density behind the shock gets low enough, $\sim 10^{11}\ \mathrm{g \cdot cm^{-3}}$, the neutrinos start to escape, contributing to further energy loss. Eventually, the shock stalls, around 100–200 km from the center (a few tens of milliseconds after bounce), near the outer iron layer. From this point, to get a successful explosion the shock must be revived within a few hundred milliseconds before the continued accretion onto the central proto neutron star (PNS) triggers further collapse into a black hole.

The exact mechanism behind the reenergization of the shock wave and the subsequent successful explosion is not fully understood [1]. The delayed neutrino heating mechanism has emerged as a promising candidate to explain the shock revival for most slowly rotating progenitors. In this scenario the intense neutrino flux from the hot PNS deposits a small fraction of its energy ($\sim$1%) into the gain region behind the stalled shock (see, e.g., Janka [22] for a review of neutrino-driven explosions). For rapidly rotating stars with strong magnetic fields (expected to account for $\sim$1% of CCSN progenitors [23]), magnetohydrodynamic effects can allow the transfer of energy from the highly magnetized PNS into the outer stellar layers for a violent explosion, in the magnetorotationally driven mechanism (e.g., [24]). While it is expected that neutrino heating plays a key role in most explosion models, the exact role of the different potential drivers of the explosion, which include the neutrino flux, differential rotation of the progenitor star, and strong magnetic fields, remains to be fully understood. We direct the reader to the review by Janka [3] for a detailed discussion of the different possible CCSN mechanisms, and to the recent review by Burrows and Vartanyan [1] and the references therein for current limitations in our understanding.

B. Gravitational waves from CCSNe

The GW signal can provide unique insight into the state of the PNS in this crucial time period, and inform about the explosion mechanism [5]. Some expected features in a GW signal are common to most CCSN models. A quadrupole moment from the deformation of the PNS is expected to occur after the core bounce. Waves from the outer convective region are likely to travel inwards and strike the outer core, and waves from convection in the PNS are likely to internally excite core and surface oscillations. For slowly rotating stars, the GW signal is then expected to be dominated by the fundamental oscillation modes of the PNS (f, g, p modes), which increase in frequency with time as the PNS contracts (e.g., [25–28]). The exact shape and amplitude of the signal can then also place constraints on the source properties such as the PNS mass, size, core compactness, and explosion energy (e.g., [29–31]).

Bulk fluid motion from the advective acoustic cycle, particularly in the gain region, may also cause global asymmetric perturbations leading to emission in the low-frequency regime. Linear or spiral oscillation modes (l, m) of the shock front may arise from the standing accretion shock instability (SASI) [32].

In the case that the explosion is powered by strong magnetic fields or amplified by a high rotation rate, prompt broadband emission can be expected within $\sim$20 ms after core bounce (e.g., [33,34]). A rapidly rotating stellar core is deformed due to its angular momentum and leads to the derivatives of the quadrupole moment to change significantly as the core collapses, and the core bounce prompt convection signal can become a dominant feature (e.g., [35,36]).

C. Detecting the GW signal with Advanced LIGO-Virgo

The stochastic nature of the CCSN explosion makes predicting exactly which features will occur currently impossible. However, the dominant emission features that are expected from the GW signals of different CCSN models, between $\sim$20 Hz–2 kHz, lie in the most sensitive frequency regime of the Advanced LIGO and Advanced Virgo detectors [14]. This sensitivity overlap makes CCSN within our Galaxy a potentially promising target for current detectors. While the expected event rate of 1–2 per century [11] for such events is low, a detection of the associated GW signal, should a Galactic CCSN happen within the next observing run, would be invaluable and could allow us to distinguish between different explosion models and mechanisms (e.g., [37,38]), as well as extract astrophysical parameters of the source progenitor and remnant.

GW detection and analysis algorithms have been developed over the years targeted toward characterizing generic short duration GW signals in the LIGO and Virgo detectors,

and some of these have been used to study GWs from CCSN. In particular, previous work by Gossan *et al.* [18] used the X-Pipeline algorithm [39] and GW waveform models from multidimensional simulations to study in detail the detectability of these models for the advanced era detectors. The recent study by Szczepańczyk *et al.* [19] used the coherent WaveBurst algorithm [40] to analyze its ability to detect and reconstruct CCSN GW signals, with an expanded and updated set of waveform models, for the anticipated fourth and fifth observing runs.

There have also been detection and inference techniques developed for analyzing the CCSN GW signal in particular, and we highlight a few studies here to show the wide range they can span. This includes the early work by Röver *et al.* [41] for the initial LIGO detectors, in which the authors used principal component analysis and Bayesian inference to reconstruct the collapse and core bounce signal, and infer properties of the PNS from the amplitudes of the principal components. Bizouard *et al.* [30] used 1D simulations to build a model for universal relations between physical properties of the compact remnant and the frequency evolution of the GW signal from PNS oscillations, and used this to estimate source properties in 2D simulations of the GW signal as would be detected by advanced era (and third generation) detectors. Similarly a CCSN detection technique developed in Astone *et al.* [42] also focused on the GWs emitted by the PNS oscillations, in this case using machine learning methods to identify the monotonically increasing signal in time-frequency spectrograms of the advanced detector network. For further examples of GW analysis techniques that have been applied to study CCSN, see Refs. [43–45].

Another candidate analysis algorithm is BayesWave, which is designed to reconstruct the signal from generic GW burst sources (short duration transient signals) using a wavelet basis, while making minimal assumptions about the specific waveform morphology [20]. This unmodeled approach, as opposed to matched filtering using known waveforms for compact binary coalescence candidates (e.g., [46–48]), makes BayesWave a suitable waveform reconstruction pipeline for CCSN studies.

To prepare for a candidate detection, we aim to study and quantify BayesWave's potential ability to reconstruct different types of CCSN signals. Furthermore we aim to identify which algorithm settings are most sensitive to CCSN signals, and produce a set of recommendations to be used for analysis on a real signal. In order to achieve these goals of characterizing BayesWave's performance, we study five different recent CCSN explosion models from three-dimensional simulations. These models encompass the same set used in Abbott *et al.* [10] and span a range of explosion models, including failed explosions, neutrino driven explosions, and magnetorotationally driven explosions.

The rest of the paper is organized as follows. In Sec. II we describe the BayesWave algorithm, the supernova waveform models we study, the general procedure for our reconstruction studies, and our optimization efforts. In Sec. III we present our results, highlighting BayesWave's reconstruction accuracy for CCSNe, gains from our optimization, and the recovery of a realistic distribution of sources in the Milky Way. Section IV follows with a discussion of BayesWave's performance between the different models, the distances to which it can reconstruct CCSN signals, and the limitations of BayesWave in this work. We summarize and conclude with final remarks and future work in Sec. V.

II. METHODS

The aim of our study is to analyze and optimize the reconstruction of CCSN GW signals with BayesWave. In the next few subsections we detail the methods that we employ, including a summary of the BayesWave algorithm and its features, a description of the CCSN waveform models selected, the steps taken to perform the reconstructions in simulated Advanced LIGO-Virgo detectors, and the optimization efforts employed in the procedure to yield more reliable and accurate reconstructions.

A. BayesWave

BayesWave is a GW signal reconstruction algorithm for short bursts that makes minimal assumptions about the signal morphology [20]. For each detector BayesWave models the analyzed data (d) as a linear combination of the GW signal in the detector frame (s), the detector's stationary Gaussian noise (n), and transient instrumental noise (glitches, g): $d = s + n + g$. The ratio of the Bayesian evidences for each model determines which has the most support.

In practice BayesWave uses a transdimensional reversible jump Markov chain Monte Carlo (RJMCMC) to place a variable number of Morlet-Gabor (sine-Gaussian) wavelets, the linear combination of which forms a reconstructed signal. For a multiple detector configuration, the wavelets placed for the signal model must be coherent across detectors, requiring the same set of extrinsic parameters (sky location, ellipticity, polarization angle) to properly project the signal onto the detectors. For the glitch model, however, the wavelets are uncorrelated.

Since the supernova analysis pipeline must make minimal assumptions about the waveform, BayesWave is then one of the more suitable choices to use in our study. Because it is agnostic to the type or source of the signal, BayesWave has been extensively used for unmodeled reconstructions of GW signals from compact binary coalescences (e.g., [49–52]) and white-noise bursts [53], as well as a glitch subtraction tool to "clean" a portion of the detector data that has an instrumental noise event overlapping with a real signal (e.g., [54,55]). It could also potentially be used as a follow-up tool to cWB to

help better discriminate CCSNe events from instrumental noise events [56].

If the analysis involves recovering a known signal that has been injected (added) into detector noise (as is the case for our study), then BayesWave also calculates the overlap (also called match) between the waveform of the injected signal h_i and the BayesWave wavelet reconstruction h_r. The overlap is defined as

$$O = \frac{(h_i|h_r)}{\sqrt{(h_i|h_i)(h_r|h_r)}}, \tag{1}$$

where the notation $(x|y)$ denotes a noise-weighted inner product using the detector's one-sided noise power spectral density $S_h(f)$:

$$(x|y) = 2\int_0^\infty \frac{x(f)y^*(f) + x^*(f)y(f)}{S_h(f)}\,df. \tag{2}$$

Thus the overlap characterizes the accuracy of the waveform reconstruction, measuring the similarity of the injected and recovered waveforms. This value ranges from -1 to 1, with $O = 1$ meaning a perfect match between the two waveforms, $O = 0$ meaning no match, and $O = -1$ indicating a perfect anticorrelation. In our work we quote the combined weighted network overlap for all $N = 3$ detectors, which is computed as

$$O_{\text{net}} = \frac{\sum_{j=1}^{N}(h_i^{(j)}|h_r^{(j)})}{\sqrt{\sum_{j=1}^{N}(h_i^{(j)}|h_i^{(j)})\sum_{j=1}^{N}(h_r^{(j)}|h_r^{(j)})}}, \tag{3}$$

where j denotes the jth detector.

In the context of our study, this means that if the BayesWave reconstructed CCSN waveform has an overlap of $O = 0.5$, for example, then that reconstructed waveform accurately matches 50% of the total time-frequency and phase signature of the true waveform. In the rest of this paper, we then often say that the reconstruction accuracy is $X\%$ to reflect the fact that the overlap value between the reconstructed and injected signals is $X/100$. Furthermore, as outlined in Sec. II C, in our studies BayesWave produces 20000 reconstructed waveforms for each injected signal, and calculates the overlap for each of these. The result is a distribution of overlap values, from which we select the median value as the characteristic overlap, and compute the standard deviation of the distribution as an estimate of the overlap uncertainty.

B. Supernova waveform models

Here we briefly describe the supernova waveform models from 3D simulations that are used in our study and the GW features they exhibit (as shown in the first row in Fig. 1). We refer the interested reader to their source papers for more detailed information about the details of their simulation procedure and modeling techniques.

(i) The O'Connor and Couch [26] *mesa20-3D-pert* model (hereafter referred to as *m20-3Dp*) has a 20 $M_\odot$ solar metallicity nonrotating progenitor star, and fails to explode within ∼500 ms after core bounce, the extent of the simulation. However, the model does emit a GW signal that is dominated by the g-mode oscillation of the PNS surface, which begins at ∼300 Hz and grows with time, peaking at ∼600–700 Hz at ∼200 ms after core bounce. A subdominant signal due to the spiral SASI modes is also present at ∼50–200 Hz.

(ii) The Radice *et al.* [27] *s9* model has a 9 $M_\odot$ solar metallicity nonrotating progenitor, and represents a lower mass neutrino-driven explosion. A broadband prompt convection signal develops ∼50 ms after bounce in conjunction with the neutrino shock breakout. After a short quiescent period, the PNS g-mode oscillation begins, rising to frequencies of ∼700 Hz. The shock is successfully revived at ∼200 ms after core bounce, and no significant GW emission occurs after ∼300 ms.

(iii) The Powell and Müller [28] *s18* model has an 18 $M_\odot$ solar metallicity nonrotating progenitor, and represents a typical neutrino driven explosion. GW emission from g-mode surface oscillations of the PNS begins ∼100 ms after core bounce, and peaks at ∼800–1000 Hz just after shock revival and onset of the explosion ∼300 ms after bounce. Significant GW emission continues up to ∼600 ms.

(iv) The Powell and Müller [57] *m39* model has a rapidly rotating Wolf-Rayet star as its progenitor with a 39 $M_\odot$ helium star mass, 2% solar metallicity, and an initial surface rotation velocity of 600 $\text{km} \cdot \text{s}^{-1}$. It is a strong neutrino driven explosion, with GW features amplified by the rapid rotation. Strong GW emission from prompt convection at low frequencies occurs shortly after bounce time, mainly visible in observer angles toward the equator. There is also a strong core bounce signal at frequencies >500 Hz. This is followed by emission associated with f-mode oscillations of the PNS, which peaks at a frequency of ∼750 Hz about 400 ms after core bounce. The shock revival occurs at ∼200 ms, and GW emission continues up to ∼600 ms.

(v) The Obergaulinger and Aloy [24] *35OC-RO* model has a 35 $M_\odot$ rapidly rotating progenitor with strong magnetic fields, with a subsolar metallicity and an equatorial surface rotation velocity of 380 $\text{km} \cdot \text{s}^{-1}$. It represents a strong magnetorotationally driven explosion. A bounce signal is quickly followed by an evolving PNS oscillation track. After the shock is revived ∼200–300 ms after bounce, the strong explosion rapidly inhibits further accretion onto the PNS, beyond which the GW signal is somewhat

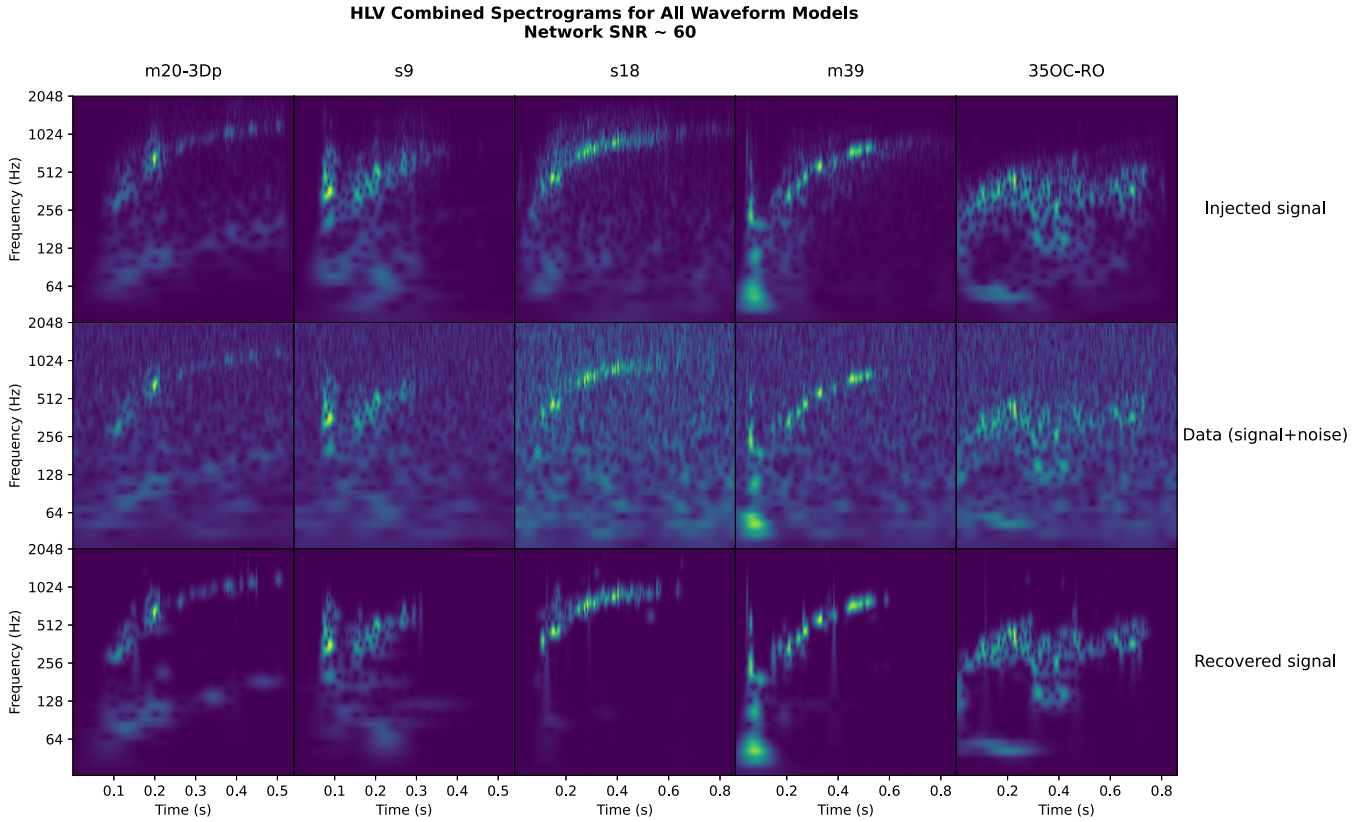

FIG. 1. The combined three detector Q-transform spectrograms for the injected signal waveform (top row), the data that BayesWave analyzes (injected signal in simulated gaussian detector noise, middle row), and the BayesWave recovered waveform (bottom row). Out of the 100 injections for each waveform model, one representative case with a relatively high network SNR ~ 60 is shown. We can see that for such loud signals, in each case BayesWave manages to recover all dominant features visible in the spectrogram, with overlap accuracies of ~80% for all waveforms. This includes the high-frequency evolving g or f mode track from the PNS oscillation, which is most easily identifiable in the s18 and m39 models, as well as the bounce and prompt convection signal which is visible in the s9 and m39 models. The 35OC-RO waveform is the most distinct with a relatively broadband track since the explosion is magnetorotationally driven instead of due to neutrino heating. Note that the timescale for the m20-3Dp and s9 waveforms is shorter than the rest (~0.5 s compared to ~0.8 s).

broadband and lasts until ~800 ms. Most of the emission occurs near frequencies of ~300–500 Hz.

C. General procedure

For each waveform model we first take the GW signal as generated by the corresponding simulation in the source frame, and project it onto the detector frame based on a given set of extrinsic parameters. This set of parameters includes the sky position of the supernova, i.e., its right ascension and declination, the distance to the source, the orientation of the source relative to the line of sight, the polarization angle of the signal, and the time of observation, which influences the detector antenna response pattern in relation to the sky position.

We generate two population sets for these parameters for each model: in the first set the sky positions follow a random uniform distribution across the whole sphere, the source orientations and polarization angles are uniform randomly distributed across all physically possible values, the time of observation is set to be 10 s apart (for a uniform-in-sky population the observation time makes no practical difference, and we choose this time for convenience), and the distances are then determined such that the resulting signal in the detector frame is log-uniform randomly distributed in SNR from 10 to 100. We produce 100 distinct signals to analyze in this way. In the second population set we change the sky positions and distances to model after a realistic spatial distribution of stars in the Milky Way galaxy, as done in Abbott *et al.* [10]. The Galaxy is modeled as a combination of the bulge, thin disk, and thick disk with parameters from the best-fitting contracted NFW halo model in Cautun *et al.* [58]. The time interval between signals is increased to 10 minutes, and a total of 150 detector signals are thus generated spanning approximately 24 hours. This is done since the detector sky antenna sensitivity pattern changes on the timescale of a day due to the rotation of the Earth, and we must account for the fact that the sources are not uniformly

distributed on the sky, but mostly lie within a narrow band that traces the Galactic disk.

These selected signals are then injected (added) into simulated Gaussian noise that is generated based on the expected design spectral noise sensitivity of the Advanced LIGO [12] and Advanced Virgo [13] detectors, taking into account the relative positions and orientations of the individual Hanford, Livingston, and Virgo detectors. The end result is a GW data file for each injected signal that has three separate channels for the strain data in each detector, mirroring what we would expect to analyze for a real signal during an observing run.

Finally, we analyze each of these signal-plus-noise data files using the BayesWave algorithm, performing waveform reconstruction of the supernova GW signal within the simulated detector noise (the injection-reconstruction process is illustrated in Fig. 1). Since BayesWave is based on a Bayesian approach to model the signal waveform and it samples the posterior distribution of the waveform parameters, for each run the output is a distribution of recovered waveforms, where each waveform represents one step in the sampler. For the runs in our study BayesWave performs a total of 4 million RJMCMC sampler iterations. To keep computational costs reasonable we then subselect and save every hundredth sample in the latter half of the run (i.e., once the distribution is steady). The BayesWave output products are then calculated based on these 20000 waveforms, and the median recovered waveform (as described in Cornish *et al.* [59]) is used as the representative final waveform. Similarly, for the network overlap we quote the median network overlap value of the 20000 waveforms, and show the 1σ standard deviation of that distribution as a measure of uncertainty on the final value wherever possible.

D. Optimizations

We aim to optimize the BayesWave run settings to maximize waveform recovery from supernovae for the different waveform models considered and across the range of possible extrinsic signal parameters. We characterize differences in performance between different run settings using the network overlap parameter [Eq. (3)], where an increase in the overlap indicates a positive gain. We consider this to be a more robust measure of whether the changes we introduce have a positive or negative impact, as compared to measuring the SNR of the recovered waveform. This is because the recovered SNR increases as BayesWave places more wavelets, regardless of whether those wavelets are capturing features appropriately. The overlap, however, appropriately penalizes any frivolously placed wavelets, focusing not simply on the excess power in the recovered signal, but on how accurately that excess power matches the shape of the true injected signal.

Since in the case of a real detection we will not know *a priori* what kind of explosion model is the underlying cause of the signal, any optimization efforts we make must be robust across all five different waveforms considered, and for the entire SNR range studied. From the potential optimizations we consider, we find two significant improvements based on: (i) knowing accurate sky localization information from electromagnetic and neutrino counterparts (e.g., [60,61]), and (ii) increasing the allowed wavelet quality factor Q, which is the number of cycles of the wavelet over one e-folding of the Gaussian envelope (i.e., describes how spread out in time it is). Thus our optimized runs correspond to setting a fixed sky location and $Q_{\max} = 100$, compared to the initial unoptimized runs with default settings in which the sky location is not fixed (uniform prior over the whole sky) and $Q_{\max} = 40$.

We also explored using frequency-evolving "chirplets" [62] instead of the fixed-frequency wavelets. However, this approach did not yield consistently positive results, and we discuss this in more detail in Sec. IV. We also note that a recent update to the BayesWave algorithm enables relaxing polarization constraints from elliptical polarization to generic polarization [59]. We were unable to fully explore this new feature for our present work, and leave a more robust analysis of its potential for CCSN signals to future studies.

Along with this we find that in order for the comparison to be appropriate and for the BayesWave runs to converge in all cases, we have to be careful of a few other run parameters. The analyzed segment length should not be less than 4 s, as below that BayesLine [63] cannot determine the spectral density of the noise accurately. The analysis window where BayesWave is allowed to place signal wavelets should be kept to approximately 1 second to make sure no part of the potential signal is being missed, and be centered on the duration of the signal (in a real scenario the "trigger" time of the event can be estimated either from low-latency GW search algorithms like coherent WaveBurst [40] or from electromagnetic or neutrino counterpart detections of CCSNe). The maximum number of allowed wavelets should scale with the SNR of the signal, where we had to set this limit to 150 wavelets for the highest SNR signals in this study. The prior on the number of wavelets should also be specified to be uniform across the allowed window of $\{1, 150\}$. The number of iterations in the RJMCMC must also not be less than 4 million, as the sampler can sometimes take at least this many steps to converge to a steady distribution, especially for higher SNR CCSN signals. Finally, we also recommend keeping the allowed frequency range wide, between ~16–32 Hz at the lower end to ~2 kHz (i.e., a maximum sampling rate of 4 kHz) at the higher end, to account for most of the features we can expect to observe from CCSN GW waveform models with current detectors.

III. RESULTS

In all subsequent sections we present our main results and figures based on the optimized BayesWave run settings

(fixed sky location, $Q_{\max} = 100$). We first show how accurate the BayesWave reconstructions are for the different types of CCSN waveform models and how this varies based on the source parameters. We then quantify and describe the increase in overlap accuracy we are able to achieve when using the optimized runs compared to the initial unoptimized runs (uniform sky prior, $Q_{\max} = 100$). This is followed by the BayesWave CCSN signal reconstruction prospects presented in the context of a population of sources modeled after the Milky Way stellar distribution.

A. Accuracy of BayesWave reconstructions

To show the potential capability of BayesWave in recovering a CCSN waveform and all its features if the signal is loud, one instance of the injection-reconstruction process and the median recovered waveform for each model is shown in Fig. 1. For each model we consider all the injections in the SNR range 55-65, and then select the one which has the median overlap value within that sample as a representative example. The features are most clearly distinguished in time-frequency spectrograms, which are plotted in Fig. 1 using a constant-Q transform [64] ($Q = 16$). Since our reconstructions are based on the three detector HLV network and BayesWave simultaneously computes the recovered waveform in all three detectors, we sum the power in the individual spectrograms after accounting for the appropriate time delay shift, and show the HLV combined spectrograms (noting that this coherent sum emphasizes the signal more over the background noise when compared to single detector signal + noise spectrograms). At such high SNRs, we can see that BayesWave is recovering all previously identified GW emission features, including the rising g or f mode PNS oscillation track visible in all models, the early broadband prompt convection in, e.g., m39, and the low-frequency SASI in m20-3Dp.

Figure 2 shows the overlap accuracy of the BayesWave reconstructed waveform for all the supernova GW signal injections analyzed in our study. The median network overlap (match) for each reconstruction in the optimized runs is plotted against the injected signal SNR for the 3 detector HLV network (root-sum-square of the individual detector SNRs). As observed in previous studies (e.g., [19]), the accuracy of the reconstruction generally increases as the signal SNR increases. Table I lists the network SNR required for each model for the network overlap to exceed 0.5 and the majority of the waveform to be recovered by BayesWave. Overall, when the SNR $\gtrsim 30$, all explosion models are confidently recovered.

However, similar to what prior work by Gossan *et al.* [18] and Szczepańczyk *et al.* [19] found for other analysis pipelines, there is a difference in BayesWave's

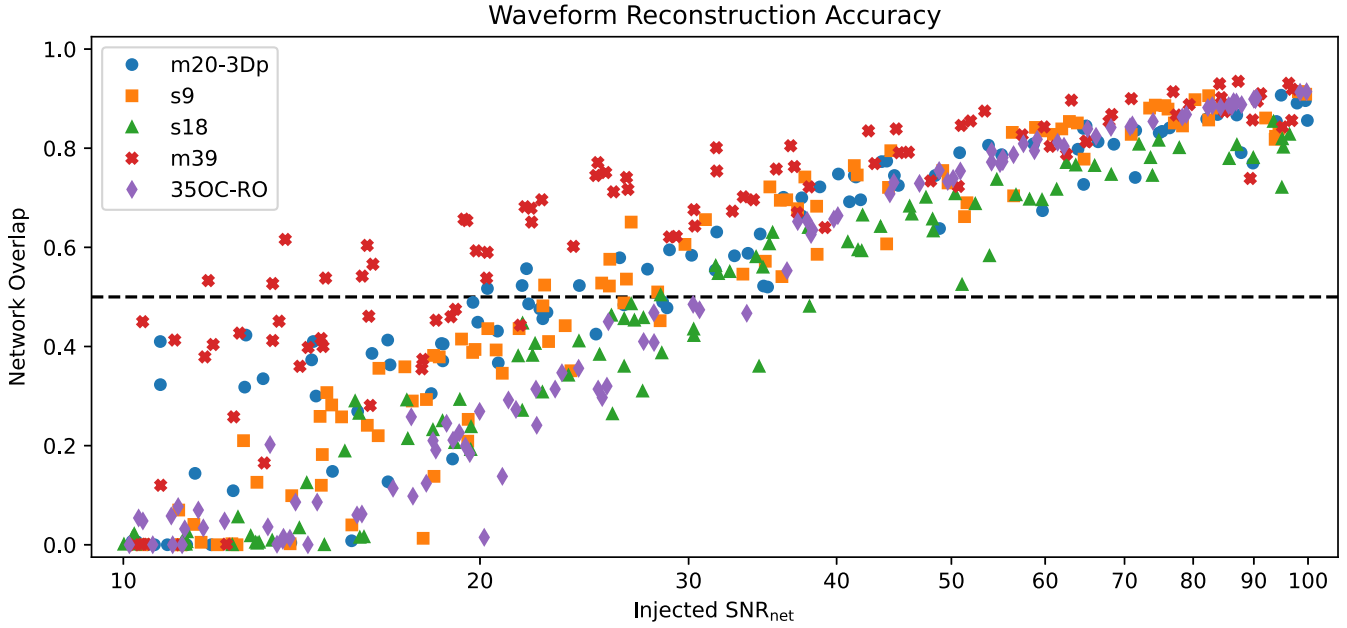

FIG. 2. A scatter plot of the BayesWave reconstructions for all the injections in the study, showing the median accuracy of the recovered waveform as measured by the network overlap (match) parameter plotted against the network SNR of the injected signal. Uncertainty error bars are omitted here for readability (see Fig. 3). The dashed black line indicates the 50% accuracy threshold. The reconstruction accuracy between models varies greatly at low SNRs, with a network SNR of $\gtrsim$30 required to exceed the 50% threshold for all models. The accuracy converges to ~90% for the highest SNR signals in this study. The differences between models can be explained by the differences in the waveform features and how compact they are in time-frequency. The scatter in the overlap accuracy for a given model near a specific SNR is a result of the small changes in the waveform morphology given varying extrinsic parameters (such as inclination angle).

TABLE I. The approximate GW signal network SNR value or source distance required for the BayesWave reconstruction network overlap value to be $O_{\rm net} \approx 0.5$ for each model. For signals with higher SNRs or lower source distances than those listed the reconstruction will have $O_{\rm net} > 0.5$, i.e., the majority of the waveform will be accurately recovered by BayesWave.

Waveform model	$\rm SNR_{net}$	Distance (kpc)
m20-3Dp	25	1.2
s9	25	0.6
s18	30	5
m39	20	40
35OC-RO	30	45

reconstruction performance between the different explosion models, especially at lower SNRs. We can see that the s18 and 35OC-RO models have the lowest accuracy, the m20-3Dp and s9 models somewhat higher, and the m39 model has the highest reconstruction accuracy (these trends are also true for the unoptimized run results, which are not shown). At higher SNRs these differences become less pronounced, with reconstruction accuracies reaching ∼90% at SNRs ∼ 100. The differences can be explained by the different waveform morphologies. How the power is distributed in time-frequency governs how well the features can be captured by BayesWave's Morlet-Gabor wavelet basis, with well-localized signals in time-frequency expected to be better reconstructed.

For each explosion model we also see that the points near a given SNR for that model have a small scatter due to different extrinsic parameters. Waveform features that BayesWave can more accurately reconstruct are a little bit more pronounced for some combination of extrinsic parameters than others that still give a similar SNR. For example, for the m39 model we know that the prompt convection signal right after core bounce is most readily observed when the line of sight is aligned with the star's equatorial plane (inclination angle = 90°) as opposed to the pole [57]. And since this feature is more compact in time-frequency as compared to the f-mode PNS oscillation track, BayesWave can recover the equatorial signals in the m39 model better than the polar ones.

Following the approach in Abbott *et al.* [10], to find out how far away a supernova source can be for BayesWave to be able to detect and reconstruct the signal in Advanced LIGO-Virgo, we show the reconstructed overlap accuracy for the injections analyzed plotted against the source distance in Fig. 3. Since each waveform model is based on very different progenitor stars and uses different modeling techniques, the total amount of energy released in the explosion—and thus in GWs—varies over a few orders of magnitude. The source distance required to have a high amplitude GW signal reach the LIGO-Virgo detectors

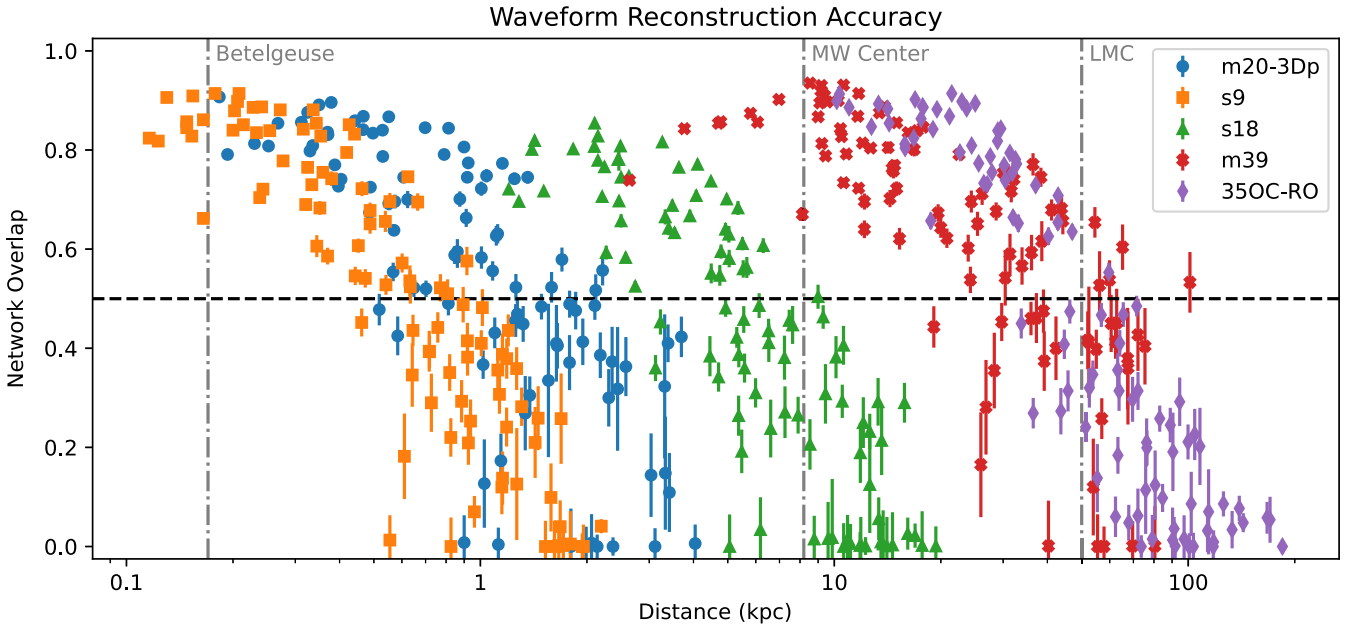

FIG. 3. The accuracy of the BayesWave recovered waveform as a function of the source distance (and explosion model) with 1σ uncertainty error bars. The dashed black line indicates the 50% accuracy threshold. Also shown for reference are three benchmark distances: Betelgeuse, the Milky Way center, and the center of the Large Magellanic Cloud. The distances at which the waveform is accurately recovered by BayesWave and passes the 50% threshold varies by almost two orders of magnitude between the different waveform models. For the low mass and relatively low explosion energy models of m20-3Dp and s9 this occurs at ∼1 kpc, for the typical neutrino-driven explosion model of s18 this is closer to the Milky Way center, and for the high explosion energy models with rapidly rotating progenitors the recoverable distances are up to the LMC at ∼50 kpc.

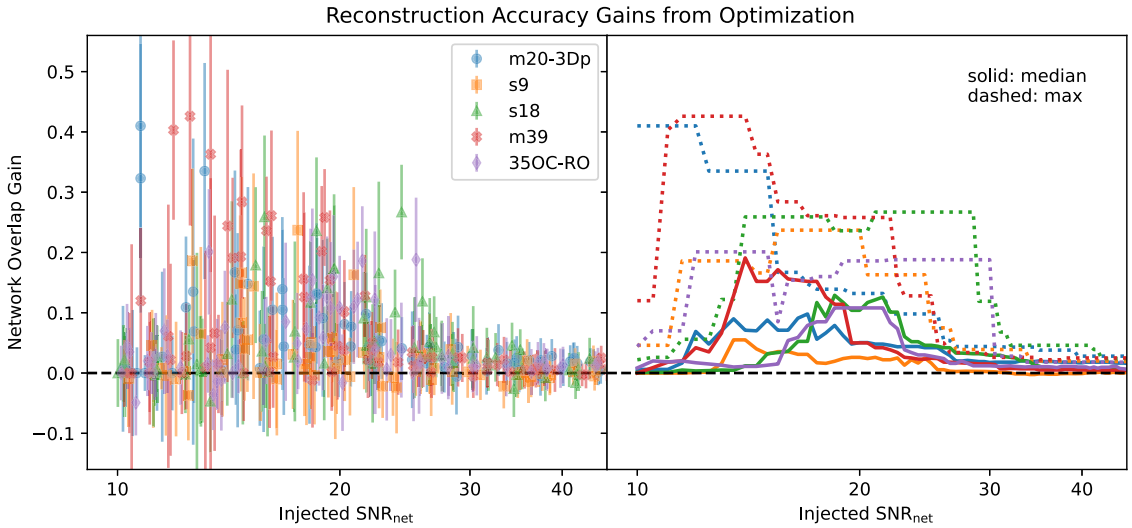

FIG. 4. The gain in the network overlap of the recovered waveform when using the optimized BayesWave run settings as compared to the initial unoptimized runs, plotted against the injected signal SNR. The scatter plot on the left shows the gains for each individual injection-reconstruction, along with the 1σ uncertainty error bars on the gain. The gains are either positive or consistent with zero. The plot on the right summarizes this information showing the median overlap gain (solid lines) and the maximum gains observed (dashed lines) near a given SNR. The median gains are on the order of ∼10% in the low SNR regime of ∼15–20, and consistent with zero for SNR $\gtrsim$ 30. The maximum observed gains can be quite large and significant, reaching an increase in overlap accuracy of about 40% for the m20-3Dp and m39 models, and more than 20% for the other three models.

is then significantly dependent on the waveform model considered (as was previously found [10,18,19]). Table I also summarizes the source distances at which the BayesWave reconstructed signal has an overlap accuracy of ∼0.5 for each waveform model, showing an almost two orders of magnitude difference between the low mass neutrino-driven explosion of the s9 model and the magnetorotationally driven explosion of the 35OC-RO model.

B. Optimization gains

In order to quantify the effects of our BayesWave optimization efforts, and to see in which cases they make the biggest impact, in Fig. 4 we plot the gain in reconstruction accuracy of the waveform between the initial and optimized BayesWave runs against the network SNR of the injected signal. The gains are most pronounced in the low SNR regime of ∼15–20, where they are typically on the order of ∼10%. However, the maximum gains observed across our study can be very high, from ∼20% for the 35OC-RO model to ∼40% for the m20-3Dp and m39 models. This SNR regime corresponds to the transition between cases where the signal is too low in amplitude for BayesWave to distinguish much of it from the detector noise, and cases where the signal is loud enough that BayesWave is starting to confidently recover most of the waveform. Thus, the optimizations are most impactful for the marginal cases, and have no significant impact for signals with SNR $\gtrsim$ 30.

A more qualitative picture of how these optimizations manifest is shown in a comparison of the time series reconstructions of the waveforms in Fig. 5. For signals with SNR ∼ 15–20 we choose the case which has the median gain in overlap within that SNR range as a representative example for each model, and show the injected and BayesWave reconstructed signals in one of the LIGO detectors (Hanford and Livingston have the same expected design sensitivity [12], so they are qualitatively interchangeable in our study). We can see that the gains in reconstruction for these examples can be attributed to a combination of BayesWave being able to: (i) find the highest amplitude part of the signal when it wasn't able to recover anything before (35OC-RO), (ii) recover the same part of the signal it was before—but more accurately (m39 and s9), and (iii) recover additional high-amplitude parts of the signal compared to only the highest amplitude portion before (s18 and m20-3Dp).

C. Prospects for a Milky Way source distribution

In Fig. 6 we show the prospects for accurate recovery of each model waveform using a realistic distribution of CCSN sources within the Milky Way galaxy, modeled according to its stellar distribution. The figure shows the histogram distribution of the network overlap in the optimized BayesWave runs for Milky Way distributed signals.

We see that for the low explosion energy models of m20-3Dp and s9, we cannot expect to reconstruct the GW signal

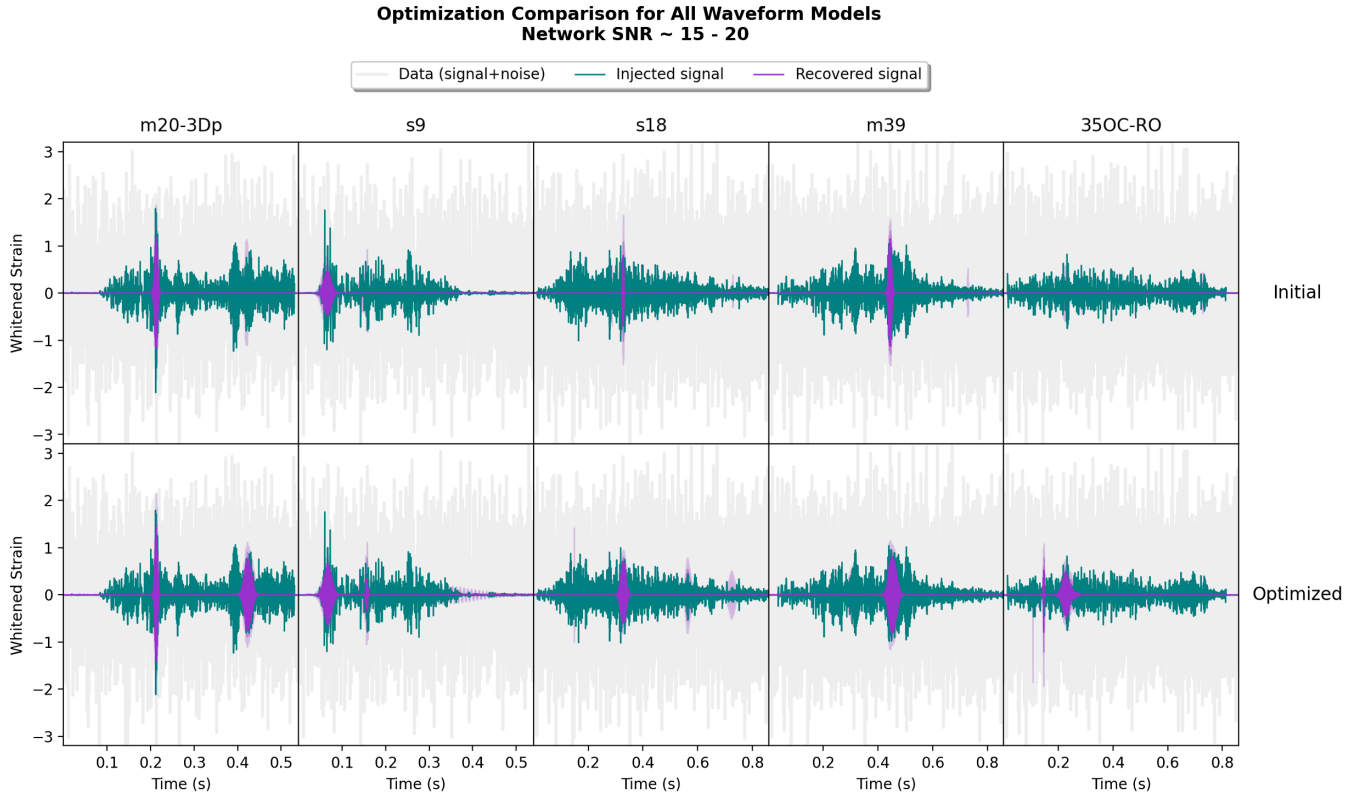

FIG. 5. The supernova waveform signals and their reconstructions in the time domain, showing the comparison between the initial BayesWave reconstructions and the optimized versions. Plotted in darkest purple is the median reconstructed waveform, while the lighter shaded bands are the 50% and 90% credible intervals. These are overlaid on top of the true injected signal, plotted in teal. To get a sense of how this signal would look like in one of the LIGO detectors, the combined signal plus detector noise is shown in gray in the background. Out of the 100 injections analyzed for each waveform model, one representative case in the low network SNR regime (∼15–20) is shown. This is the SNR range where the optimizations lead to the highest gains in reconstruction accuracy, as seen in Fig. 4. We can see that the gains in reconstruction can generally be attributed to BayesWave's ability to more confidently and accurately capture the high-amplitude features. Note that the timescale for the m20-3Dp and s9 waveforms is shorter than the rest (∼0.5 s compared to ∼0.8 s).

in almost all cases (the overlap is nonzero for $< 5\%$ of sources), consistent with what Abbott *et al.* [10] find. This is primarily because the stellar distribution in the Galaxy is most concentrated toward the central bulge near 8 kpc, while we see in Fig. 3 that these models are not confidently recovered beyond ∼1–2 kpc.

For the s18 model we have a somewhat broader distribution, with a nonzero overlap in ∼65% of cases, and a confident reconstruction with overlap >0.5 for ∼15% of the sources. The most likely (nonzero) overlap value, coincident with sources at the Galactic center, is ∼0.3. Due to the fact that our optimizations were largely effective at lower SNRs, and this SNR regime is coincident with sources near the Galactic center for the s18 model, it is also the only model for which we see a measurable increase in the percentage of cases that are recovered between the unoptimized and optimized runs: a 5% increase from 11% to 16% for confident reconstructions, and a 15% increase from 52% to 67% for nonzero overlap.

For the two high explosion energy models, we see that $>95\%$ of cases have overlap >0.5. The most likely overlap, coincident with sources at the center of the Milky Way, is ∼0.85 for m39 and ∼0.95 for 35OC-RO. In Fig. 7 in the appendix we also show the spectrograms for the most likely reconstruction for sources at the Galactic center for each waveform model.

IV. DISCUSSION

A. Reconstruction accuracy model dependence

The duration of the GW emission plays a central role in influencing the quality of the BayesWave reconstruction. Since the SNR is an integrated measure of the signal power across the analyzed segment, when comparing different model injections at a fixed SNR, their total power is the same. However, the injected signals in Fig. 1 show that significant GW emissions last for about 0.5 s for s18 and about 0.7 s for the 35OC-RO model, making them more spread out in time compared to the ∼0.3 s emissions from m20-3Dp and s9. On average, this effectively distributes the signal power so that analyzing a similar 0.3 second segment in the longer models would have about half the

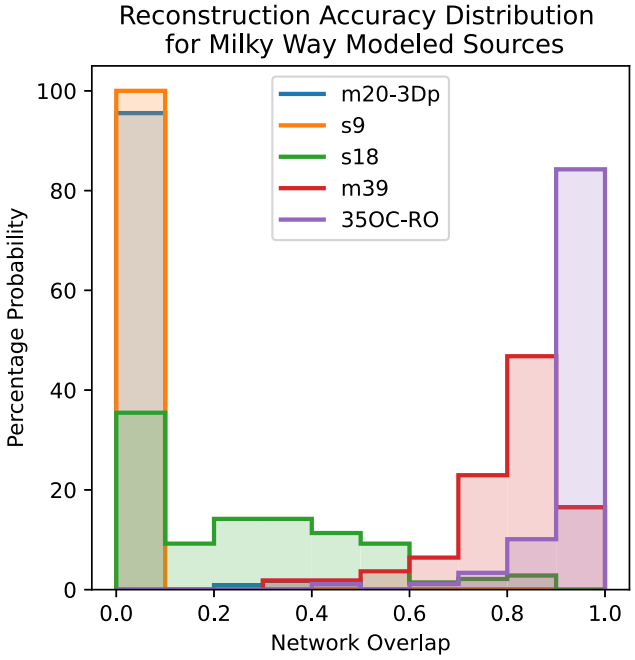

FIG. 6. The histogram distribution of the optimized BayesWave reconstructed network overlap for each supernova model, for a population of injections with extrinsic parameters modeled according to a realistic distribution of stars in the Milky Way. We see that for such a distribution, we do not expect to be able to recover the GW waveform with BayesWave from low energy m20-3Dp- or s9-like supernova models. For more typical neutrino-driven explosion models like s18, BayesWave can recover a nonzero overlap in many cases, but high accuracy reconstructions with overlap >0.5 occur only in ∼15% of cases. For stronger explosions in the Galaxy from rapidly rotating progenitors (m39, 35OC-RO), almost all of them can be expected to be confidently and accurately recovered.

power as compared to the shorter ones. Since BayesWave places wavelets in time-frequency trying to capture this localized power wherever it confidently can [20], the wavelet basis better captures signals that have their excess power concentrated in a shorter time (following the same reasoning as to why high mass compact binary coalescences are better reconstructed compared to low mass ones in Ghonge *et al.* [51]). For the m39 model, even though it is one of the longer duration models with significant GW emissions lasting about 0.6 s, depending on the source orientation it often produces much of that excess power in the short duration early rotational bounce signal (seen in Fig. 1), which BayesWave easily recovers.

Compactness in frequency of the GW emission further explains differences in reconstruction accuracy. For example, in the m39 model the f-mode PNS oscillation track is very narrow in time-frequency. Compare this to the s18 model where no high amplitude prompt convection mechanism contributes and the signal energy is distributed throughout a relatively broader PNS g-mode oscillation track (as well as what seems to be a low-frequency persistent background component), making it harder for BayesWave to recover. The other three models are similarly more spread out in frequency than m39, negatively affecting the ability of the compact Morlet-Gabor wavelets to capture this more broadband power.

At lower SNRs these differences in the reconstruction accuracy are more pronounced because BayesWave needs the localized SNR in each segment of the signal to be above a certain threshold to justify placing a wavelet there (since it takes a Bayesian approach, the increase in signal likelihood must exceed the Occam factor penalty for increasing the signal model complexity [20,65,66]). Capturing localized excess is then only possible close to where the signal amplitude peaks for lower SNR signals (as seen in Fig. 5), which varies significantly from model to model. On the other hand, for high SNR signals the signal amplitude is high enough to be distinguished from the noise across the whole waveform, and so BayesWave can place wavelets across the signal relatively unaffected by the specific distribution of the power.

In future work we plan to do a deeper investigation on the possibility of distinguishing between the different model features, and potentially extracting physical parameters of the progenitor, using machine learning techniques on the waveform reconstructions that BayesWave outputs.

B. Reconstruction distances in context

In Fig. 3, along with presenting the distance dependence of the BayesWave reconstructions for the optimized runs, we also include distances to some common benchmarks for comparison, similar to Fig. 7 in Abbott *et al.* [10]. Betelgeuse is the nearest red supergiant to Earth, expected to end its life in a CCSN [67]. The Milky Way center is the region with the highest density of massive stars in the Galaxy, and so it is the most likely source for the next Galactic supernova. The Large Magellanic Cloud is the host galaxy to supernova 1987A, one of the most recent and closest CCSN observed, and the only one also detected with neutrinos [6–8]. We see that for the low explosion energy models of s9 and m20-3Dp, the GW waveform is very well recovered by BayesWave at distances close to Betelgeuse, but the accuracy falls below the 50% threshold very quickly beyond ∼1–2 kpc. The typical neutrino driven explosion of model s18 is recovered well at galactic distances, up to the center of the Milky Way, but cannot be recovered for sources beyond our galaxy. For the very highest explosion energy models of m39 and 35OC-RO however, the BayesWave reconstruction has accuracies of ∼90% close to the Milky Way center, and is well recovered even up to the LMC. If Betelgeuse goes supernova during the advanced detector era then we can see that BayesWave will accurately recover and reconstruct almost all of the

GW signal, regardless of waveform model (even if the explosion is not successful, as in the m20-3Dp model).

These distances are also significantly larger than the detection distances found for the same set of waveform models studied with BayesWave in Abbott *et al.* [10], as shown in Fig. 7 of their paper. This is expected, as the LVK study is based on the actual detector noise curves recorded for the LIGO and Virgo detectors during the third observing run, which is roughly a factor of 1.5 less sensitive than the design Advanced LIGO-Virgo configuration that we use in this study, in anticipation of the fourth observing run [14]. Note that there is also a difference in the distance measure analyzed: the LVK study quotes the distance at which 50% (and 10%) of the total injections are detected, whereas in our study we look at the distance at which the recovered waveform accuracy is on average 50%. We also find that the BayesWave reconstruction overlap accuracies at given distances (and SNRs) for the Advanced LIGO-Virgo detectors are broadly consistent with those reported by Szczepańczyk *et al.* [19] using the coherent WaveBurst algorithm.

As was done for the third observing run sensitivity in Abbott *et al.* [10], for a realistic distribution of CCSN progenitors within the Milky Way we have also quantified the prospects for BayesWave to confidently reconstruct the emitted GW signal for the expected sensitivities in the fourth observing run (Fig. 6). This also demonstrates how the distribution of sources within the Galaxy modulates the detectability of each supernova model, as most stars are concentrated near the center of the Galaxy ~ 8 kpc away from the Sun. Should the next Galactic CCSN be a low energy or failed explosion, we do not anticipate being able to detect it in Advanced LIGO-Virgo with BayesWave (unless we are very lucky and the source is $\lesssim 1$ kpc away). If it is a typical neutrino driven explosion like the s18 model however, we expect that there is a $\sim$65% chance BayesWave will recover a part of the GW signal, and a $\sim$15% chance it will be confidently reconstructed. Finally, if the explosion follows from a rapidly rotating progenitor, then BayesWave will almost certainly recover the GW features confidently (>95% probability). However, such rapid rotation is only expected to occur in $\sim$1% of all CCSN progenitors [23].

C. Limits to BayesWave reconstructions

The work by Pannarale *et al.* [68] characterizes BayesWave's performance in general from a theoretical approach, and suggests a formulation for the maximum possible overlap (match) in Eq. (8) of their paper. We test this prediction against our CCSN reconstructions for all five of the waveform models studied, and plot the difference between the two for our optimized runs in Fig. 8 (included in the appendix). What we see is similar to what Pannarale *et al.* [68] find, which is that more complicated and longer waveforms (such as the 35OC-RO model in our study) show a larger disparity with the predictions and have a harder time reaching that theoretical maximum as compared to waveforms that are more compact in time-frequency (such as the m39 model). This also explains why BayesWave has a harder time recovering the signal accurately from all of the supernova models in our study, when compared to its performance in recovering the signal from coalescing binary black holes as studied in Pannarale *et al.* [68].

The disparity between the predicted overlaps and the CCSN overlaps in our study also shows an SNR dependence, where the predictions overestimate much more at lower SNRs than at higher. This happens because Pannarale *et al.* [68] state that Equation 8 is valid in the limit that the squared SNR recovered per pixel (wavelet) is much greater than unity, which is a requirement that holds true for reconstruction of high SNR signals in our study, but becomes more tenuous for lower SNR signal reconstructions. Theoretically we are expecting that there should be some useful information, but practically at such SNRs the signal is buried in Gaussian noise and BayesWave has a very hard time extracting any part of it, giving very little or no information.

We also consider the limits of BayesWave to understand why our run optimization efforts work well at relatively lower SNRs. When the signals are not very loud, BayesWave's certainty in determining the time delay of certain signal features between the three different detectors decreases, and so the reconstructed sky localization is not accurate, with the 90% confidence sky area not constrained to better than ~ 50 deg^2 for SNR $\lesssim 30$. This increase in the posterior distribution for the source sky position parameter is associated with a decrease in the calculated likelihood when placing a wavelet to capture that signal feature, and so in the RJMCMC BayesWave places a wavelet to capture that power less often, resulting in a lower median overlap. When the true sky position is known and fixed however, the parameter space is significantly reduced, and so BayesWave places wavelets at the corresponding signal feature locations much more confidently, and thus much more often, increasing the median overlap.

The increase in overlap due to a higher wavelet quality factor is a direct result of the fact that supernova waveforms generally have high amplitude features that are spread out in time, and so longer duration wavelets are required to capture the power not just at the precise time where the amplitude is large, but also in its immediate vicinity (as illustrated in Fig. 5). At higher SNRs this makes little difference, as instead of having to capture the excess power using only one wavelet, the signal is loud enough that BayesWave can confidently place many wavelets to capture the same power.

In our optimization efforts during our study we had also considered using frequency-evolving "chirplets" [62] instead of the fixed-frequency wavelets, i.e., increasing the

allowed waveform complexity in a bid to capture the nuances in the signal morphologies more accurately. However, this was not included in the final optimized BayesWave runs as it did not yield positive gains for all the different waveform models. While using chirplets increased the overlap accuracy by ∼5% for low SNR signals for the more broadband 35OC-RO model, it also resulted in a slight net negative overlap at low SNRs for the m20-3Dp and m39 models (while having no measurable impact on the other two models). Combined with the fact that the computing time is almost twice as long for the chirplet model as compared to the wavelet, we recommend that the wavelet model be used for supernova analysis unless the signal is known to be broadband from other analyses.

V. CONCLUSION

Core-collapse supernova explosion models predict the production of gravitational waves within the first second after core-collapse, exhibiting dominant emission features with frequencies that lie in the most sensitive regime of current interferometric ground based detectors. Galactic CCSNe represent a rare but promising astrophysical source that could be detected by the Advanced LIGO and Advanced Virgo detectors in one of their upcoming observing runs.

In order to prepare for such a detection, in this paper we study how well the BayesWave algorithm can reconstruct the GW signal emitted by a range of different explosion models with different waveform morphologies, if such a signal is detected by a design sensitivity LIGO-Virgo network configuration. We also optimize the BayesWave run settings for CCSNe, focusing on maximizing the reconstruction overlap accuracy, and provide a set of recommendations for the run settings for analysis on a real candidate signal.

We find that BayesWave's reconstruction performance varies depending on the complexity of the waveform, with models that exhibit features that are more compact in time-frequency being better recovered than models that have their power distributed over a longer time and have broadband emission, consistent with previous work [19]. With that said, BayesWave can confidently recover the GW signal from a range of supernova explosion models in Advanced LIGO-Virgo for network SNR $\gtrsim 30$, with maximum accuracies of ∼90% for SNR ~ 100, as shown in Fig. 2.

The corresponding distances, as seen in Fig. 3, are from as low as ∼1 kpc for low mass neutrino driven explosions, to up to ∼50 kpc for high mass magnetorotationally driven explosions. We put this into context of what percentage of CCSN within our Galaxy we could confidently recover with BayesWave by also studying the reconstructions for a realistic distribution of stellar sources in the Miky Way (Fig. 6). We find that should the next Galactic CCSN be a low mass or failed explosion, BayesWave is likely to not detect it. However, there is a ∼15% chance that the source is close enough that for typical neutrino driven explosions like the s18 model, BayesWave will be able to confidently reconstruct the GW emission. Should a high energy CCSN from a rapidly rotating progenitor be the source, BayesWave will confidently recover the GW signal in >95% of cases.

A key result of our work is that optimizing the BayesWave run settings increases the reconstructed accuracy significantly for low SNR signals, with gains of up to ∼20–40% for lower SNR signals, and typically ∼10% in the SNR ∼ 15–20 regime, as shown in Fig. 4. These gains are based on: (i) exploiting the multimessenger nature of CCSNe so that the sky location is known from the electromagnetic and neutrino counterpart observations, allowing BayesWave to more confidently recover waveform features, and (ii) increasing the allowed wavelet quality factor (to $Q_{\max} = 100$) so that high amplitude features that are more spread out in time for supernova signals are more accurately reconstructed. For typical neutrino-driven explosions like the s18 model, this also translates into being able to recover the signal from ∼15% more sources in our Galaxy.

Our results show that if there is a CCSN signal detection in Advanced LIGO-Virgo, for loud enough signals the BayesWave algorithm will be able to accurately reconstruct the dominant GW emission features, regardless of the specific model. This will help us distinguish between different supernova explosion models and mechanisms, and allow crucial insight into the dynamics of the very first second of the explosion.

ACKNOWLEDGMENTS

The authors gratefully acknowledge Jade Powell, Meg Millhouse, Katerina Chatziioannou, Tyson Littenberg, Bence Bécsy, Sudarshan Ghonge and Evan Goetz for useful discussions related to this work. The manuscript has benefited from internal LVK collaboration review under the document ID P2100404. This material is based upon work supported by NSF's LIGO Laboratory which is a major facility fully funded by the National Science Foundation. The authors gratefully acknowledge the support of the NSF for provision of computational resources. This research is funded by an NSERC Discovery Grant. G. D. is supported through the iBOF-project BOF20/IBF/124.

APPENDIX: SUPPLEMENTARY FIGURES

To supplement the discussion in the main text, in Fig. 7 we show spectrograms for the most likely BayesWave reconstruction for sources near the Galactic center for each waveform model. For each model we consider all the injections from the Milky Way distributed population, in the distance range 7–9 kpc, and then select the one which

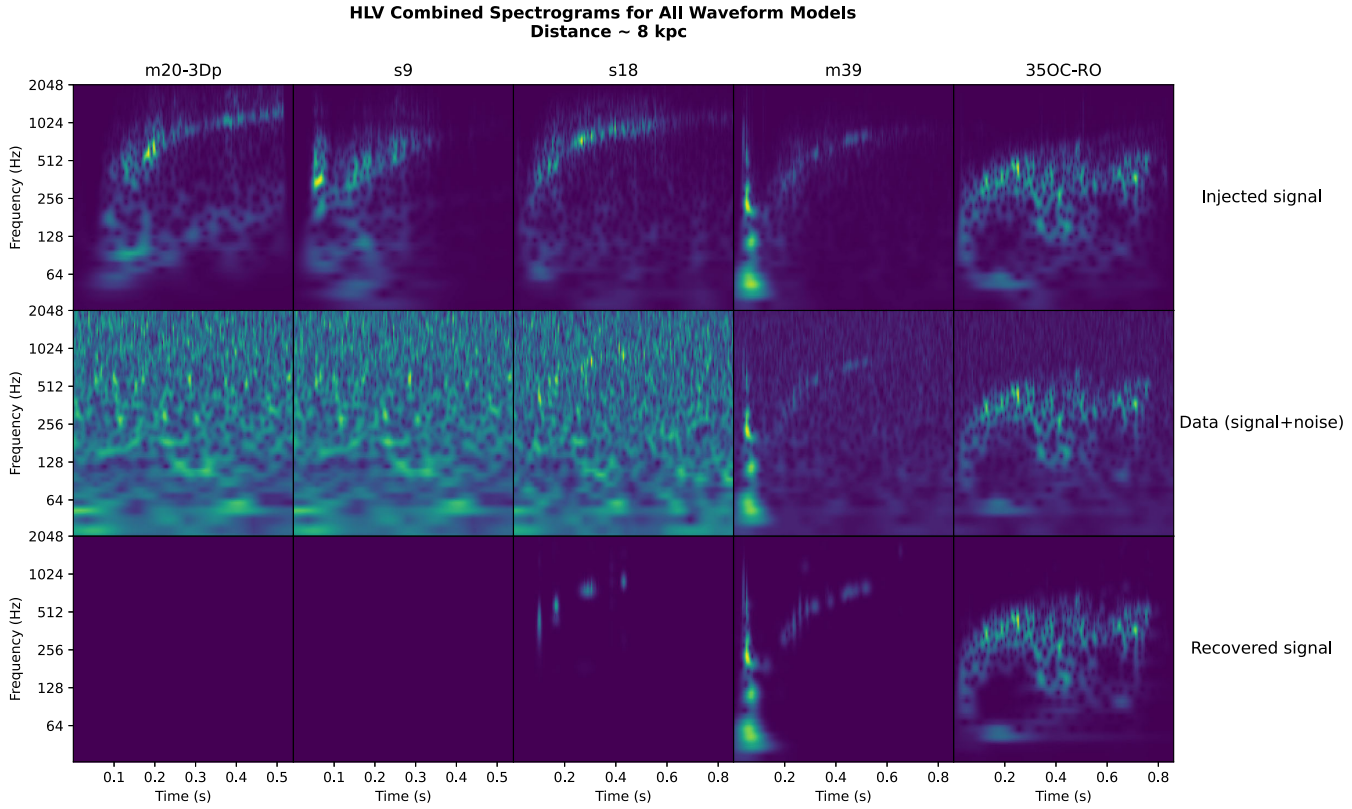

FIG. 7. The combined three detector Q-transform spectrograms for the injected signal waveform (top row), the data that BayesWave analyzes (injected signal in simulated Gaussian detector noise, middle row), and the BayesWave recovered waveform (bottom row). Out of the 150 Milky Way distributed injections for each waveform model, one representative case at the Galactic center at a distance of ~8 kpc is shown. The m20-3Dp and s9 waveforms are not reconstructed at all, the s18 model has an overlap reconstruction accuracy of ~30%, the m39 model has an accuracy of ~85%, and the 35OC-RO model has an accuracy of ~95%. The large differences in accuracy of reconstructions are due to the differences in GW amplitude and energy between models.

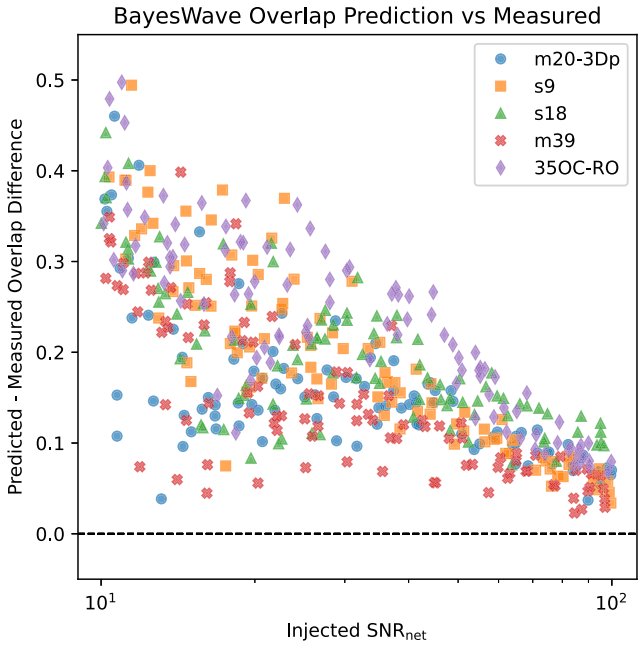

FIG. 8. Comparison of the theoretical predictions of the BayesWave overlap according to Eq. (8) in Pannarale *et al.* [68], and the measured overlap in our study. Our measurements are worse than the predicted values (as expected), and quantify how the prediction breaks down for longer duration signals like CCSNe. The mismatch is larger for lower SNR signals, and generally larger for models that have more complex features in time-frequency such as the 35OC-RO model.

has the median overlap value within that sample as a representative example.

We also test the predictions made in the work by Pannarale *et al.* [68] characterizing BayesWave's performance from a theoretical approach, against our CCSN reconstructions for all five of the waveform models studied, and the difference between the two for our optimized runs is shown in Fig. 8.

[1] A. Burrows and D. Vartanyan, Core-collapse supernova explosion theory, Nature (London) **589**, 29 (2021).

[2] M. D. Kistler, W. C. Haxton, and H. Yüksel, Tomography of massive stars from core collapse to supernova shock breakout, Astrophys. J. **778**, 81 (2013).

[3] H.-T. Janka, Explosion mechanisms of core-collapse supernovae, Annu. Rev. Nucl. Part. Sci. **62**, 407 (2012).

[4] B. Müller, Neutrino emission as diagnostics of core-collapse supernovae, Annu. Rev. Nucl. Part. Sci. **69**, 253 (2019).

[5] E. Abdikamalov, G. Pagliaroli, and D. Radice, Gravitational waves from core-collapse supernovae, arXiv:2010.04356.

[6] K. Hirata *et al.*, Observation of a Neutrino Burst from the Supernova SN1987A, Phys. Rev. Lett. **58**, 1490 (1987).

[7] R. M. Bionta *et al.*, Observation of a Neutrino Burst in Coincidence with Supernova 1987A in the Large Magellanic Cloud, Phys. Rev. Lett. **58**, 1494 (1987).

[8] E. N. Alexeyev, L. N. Alexeyeva, I. V. Krivosheina, and V. I. Volchenko, Detection of the neutrino signal from SN 1987A in the LMC using the INR Baksan underground scintillation telescope, Phys. Lett. B **205**, 209 (1988).

[9] B. P. Abbott *et al.* (LIGO Scientific Collaboration and Virgo Collaboration), Optically targeted search for gravitational waves emitted by core-collapse supernovae during the first and second observing runs of advanced LIGO and advanced Virgo, Phys. Rev. D **101**, 084002 (2020).

[10] R. Abbott *et al.* (The LIGO Scientific Collaboration, the Virgo Collaboration, and the KAGRA Collaboration), All-sky search for short gravitational-wave bursts in the third Advanced LIGO and Advanced Virgo run, Phys. Rev. D **104**, 122004 (2021).

[11] K. Rozwadowska, F. Vissani, and E. Cappellaro, On the rate of core collapse supernovae in the milky way, New Astron. **83**, 101498 (2021).

[12] J. Aasi *et al.* (LIGO Scientific Collaboration), Advanced LIGO, Classical Quantum Gravity **32**, 074001 (2015).

[13] F. Acernese *et al.* (Virgo Collaboration), Advanced Virgo: A second-generation interferometric gravitational wave detector, Classical Quantum Gravity **32**, 024001 (2015).

[14] B. P. Abbott *et al.* (Kagra Collaboration, LIGO Scientific Collaboration, and VIRGO Collaboration), Prospects for observing and localizing gravitational-wave transients with Advanced LIGO, Advanced Virgo and KAGRA, Living Rev. Relativity **23**, 3 (2020).

[15] K. Somiya, Detector configuration of KAGRA-the Japanese cryogenic gravitational-wave detector, Classical Quantum Gravity **29**, 124007 (2012).

[16] Y. Aso, Y. Michimura, K. Somiya, M. Ando, O. Miyakawa, T. Sekiguchi, D. Tatsumi, and H. Yamamoto, Interferometer design of the KAGRA gravitational wave detector, Phys. Rev. D **88**, 043007 (2013).

[17] B. Iyer *et al.*, LIGO-India, Technical Report No. M1100296-v2, IndIGO, India, 2011.

[18] S. E. Gossan, P. Sutton, A. Stuver, M. Zanolin, K. Gill, and C. D. Ott, Observing gravitational waves from core-collapse supernovae in the advanced detector era, Phys. Rev. D **93**, 042002 (2016).

[19] M. J. Szczepańczyk *et al.*, Detecting and reconstructing gravitational waves from the next galactic core-collapse supernova in the advanced detector era, Phys. Rev. D **104**, 102002 (2021).

[20] N. J. Cornish and T. B. Littenberg, Bayeswave: Bayesian inference for gravitational wave bursts and instrument glitches, Classical Quantum Gravity **32**, 135012 (2015).

[21] S. E. Woosley, A. Heger, and T. A. Weaver, The evolution and explosion of massive stars, Rev. Mod. Phys. **74**, 1015 (2002).

[22] H.-T. Janka, Neutrino-driven explosions, in *Handbook of Supernovae*, edited by A. W. Alsabti and P. Murdin (Springer International Publishing, New York, 2017), p. 1095.

[23] S. E. Woosley and A. Heger, The progenitor stars of gamma-ray bursts, Astrophys. J. **637**, 914 (2006).

[24] M. Obergaulinger and M. Á. Aloy, Magnetorotational core collapse of possible GRB progenitors—I. Explosion mechanisms, Mon. Not. R. Astron. Soc. **492**, 4613 (2020).

[25] A. Torres-Forné, P. Cerdá-Durán, A. Passamonti, and J. A. Font, Towards asteroseismology of core-collapse supernovae with gravitational-wave observations—I. Cowling approximation, Mon. Not. R. Astron. Soc. **474**, 5272 (2018).

[26] E. P. O'Connor and S. M. Couch, Exploring fundamentally three-dimensional phenomena in high-fidelity simulations of core-collapse supernovae, Astrophys. J. **865**, 81 (2018).

[27] D. Radice, V. Morozova, A. Burrows, D. Vartanyan, and H. Nagakura, Characterizing the gravitational wave signal from core-collapse supernovae, Astrophys. J. Lett. **876**, L9 (2019).

[28] J. Powell and B. Müller, Gravitational wave emission from 3D explosion models of core-collapse supernovae with low and normal explosion energies, Mon. Not. R. Astron. Soc. **487**, 1178 (2019).

[29] A. Torres-Forné, P. Cerdá-Durán, M. Obergaulinger, B. Müller, and J. A. Font, Universal Relations for Gravitational-Wave Asteroseismology of Protoneutron Stars, Phys. Rev. Lett. **123**, 051102 (2019).

[30] M.-A. Bizouard, P. Maturana-Russel, A. Torres-Forné, M. Obergaulinger, P. Cerdá-Durán, N. Christensen, J. A. Font,

and R. Meyer, Inference of protoneutron star properties from gravitational-wave data in core-collapse supernovae, Phys. Rev. D **103**, 063006 (2021).
[31] H. Sotani, T. Takiwaki, and H. Togashi, Universal relation for supernova gravitational waves, Phys. Rev. D **104**, 123009 (2021).
[32] J. M. Blondin, A. Mezzacappa, and C. DeMarino, Stability of standing accretion shocks, with an eye toward core-collapse supernovae, Astrophys. J. **584**, 971 (2003).
[33] T. Takiwaki and K. Kotake, Gravitational wave signatures of magnetohydrodynamically driven core-collapse supernova explosions, Astrophys. J. **743**, 30 (2011).
[34] S. Richers, C. D. Ott, E. Abdikamalov, E. O'Connor, and C. Sullivan, Equation of state effects on gravitational waves from rotating core collapse, Phys. Rev. D **95**, 063019 (2017).
[35] E. Abdikamalov, S. Gossan, A. M. DeMaio, and C. D. Ott, Measuring the angular momentum distribution in core-collapse supernova progenitors with gravitational waves, Phys. Rev. D **90**, 044001 (2014).
[36] J. Fuller, H. Klion, E. Abdikamalov, and C. D. Ott, Supernova seismology: Gravitational wave signatures of rapidly rotating core collapse, Mon. Not. R. Astron. Soc. **450**, 414 (2015).
[37] J. Logue, C. D. Ott, I. S. Heng, P. Kalmus, and J. H. C. Scargill, Inferring core-collapse supernova physics with gravitational waves, Phys. Rev. D **86**, 044023 (2012).
[38] V. Roma, J. Powell, I. S. Heng, and R. Frey, Astrophysics with core-collapse supernova gravitational wave signals in the next generation of gravitational wave detectors, Phys. Rev. D **99**, 063018 (2019).
[39] P. J. Sutton, G. Jones, S. Chatterji, P. Kalmus, I. Leonor, S. Poprocki, J. Rollins, A. Searle, L. Stein, M. Tinto, and M. Was, X-Pipeline: An analysis package for autonomous gravitational-wave burst searches, New J. Phys. **12**, 053034 (2010).
[40] S. Klimenko, G. Vedovato, M. Drago, F. Salemi, V. Tiwari, G. A. Prodi, C. Lazzaro, K. Ackley, S. Tiwari, C. F. Da Silva, and G. Mitselmakher, Method for detection and reconstruction of gravitational wave transients with networks of advanced detectors, Phys. Rev. D **93**, 042004 (2016).
[41] C. Röver, M.-A. Bizouard, N. Christensen, H. Dimmelmeier, I. S. Heng, and R. Meyer, Bayesian reconstruction of gravitational wave burst signals from simulations of rotating stellar core collapse and bounce, Phys. Rev. D **80**, 102004 (2009).
[42] P. Astone, P. Cerdá-Durán, I. Di Palma, M. Drago, F. Muciaccia, C. Palomba, and F. Ricci, New method to observe gravitational waves emitted by core collapse supernovae, Phys. Rev. D **98**, 122002 (2018).
[43] K. Hayama, T. Kuroda, K. Kotake, and T. Takiwaki, Coherent network analysis of gravitational waves from three-dimensional core-collapse supernova models, Phys. Rev. D **92**, 122001 (2015).
[44] V. Srivastava, S. Ballmer, D. A. Brown, C. Afle, A. Burrows, D. Radice, and D. Vartanyan, Detection prospects of core-collapse supernovae with supernova-optimized third-generation gravitational-wave detectors, Phys. Rev. D **100**, 043026 (2019).
[45] J. Powell and B. Müller, Inferring astrophysical parameters of core-collapse supernovae from their gravitational-wave emission, Phys. Rev. D **105**, 063018 (2022).
[46] T. Adams, D. Buskulic, V. Germain, G. M. Guidi, F. Marion, M. Montani, B. Mours, F. Piergiovanni, and G. Wang, Low-latency analysis pipeline for compact binary coalescences in the advanced gravitational wave detector era, Classical Quantum Gravity **33**, 175012 (2016).
[47] S. A. Usman *et al.*, The PyCBC search for gravitational waves from compact binary coalescence, Classical Quantum Gravity **33**, 215004 (2016).
[48] C. Messick *et al.*, Analysis framework for the prompt discovery of compact binary mergers in gravitational-wave data, Phys. Rev. D **95**, 042001 (2017).
[49] K. Chatziioannou, J. A. Clark, A. Bauswein, M. Millhouse, T. B. Littenberg, and N. Cornish, Inferring the post-merger gravitational wave emission from binary neutron star coalescences, Phys. Rev. D **96**, 124035 (2017).
[50] B. P. Abbott *et al.* (LIGO Scientific Collaboration and Virgo Collaboration), GWTC-1: A Gravitational-Wave Transient Catalog of Compact Binary Mergers Observed by LIGO and Virgo during the First and Second Observing Runs, Phys. Rev. X **9**, 031040 (2019).
[51] S. Ghonge, K. Chatziioannou, J. A. Clark, T. Littenberg, M. Millhouse, L. Cadonati, and N. Cornish, Reconstructing gravitational wave signals from binary black hole mergers with minimal assumptions, Phys. Rev. D **102**, 064056 (2020).
[52] G. Dálya, P. Raffai, and B. Bécsy, Bayesian reconstruction of gravitational-wave signals from binary black holes with nonzero eccentricities, Classical Quantum Gravity **38**, 065002 (2021).
[53] B. Bécsy, P. Raffai, N. J. Cornish, R. Essick, J. Kanner, E. Katsavounidis, T. B. Littenberg, M. Millhouse, and S. Vitale, Parameter estimation for gravitational-wave bursts with the BayesWave pipeline, Astrophys. J. **839**, 15 (2017).
[54] C. Pankow, K. Chatziioannou, E. A. Chase, T. B. Littenberg, M. Evans, J. McIver, N. J. Cornish, C.-J. Haster, J. Kanner, V. Raymond, S. Vitale, and A. Zimmerman, Mitigation of the instrumental noise transient in gravitational-wave data surrounding GW170817, Phys. Rev. D **98**, 084016 (2018).
[55] K. Chatziioannou, N. Cornish, M. Wijngaarden, and T. B. Littenberg, Modeling compact binary signals and instrumental glitches in gravitational wave data, Phys. Rev. D **103**, 044013 (2021).
[56] K. Gill, W. Wang, O. Valdez, M. Szczepanczyk, M. Zanolin, and S. Mukherjee, Enhancing the sensitivity of searches for gravitational waves from core-collapse supernovae with a Bayesian classification of candidate events, arXiv:1802.07255.
[57] J. Powell and B. Müller, Three-dimensional core-collapse supernova simulations of massive and rotating progenitors, Mon. Not. R. Astron. Soc. **494**, 4665 (2020).
[58] M. Cautun, A. Benítez-Llambay, A. J. Deason, C. S. Frenk, A. Fattahi, F. A. Gómez, R. J. J. Grand, K. A. Oman, J. F. Navarro, and C. M. Simpson, The milky way total mass profile as inferred from Gaia DR2, Mon. Not. R. Astron. Soc. **494**, 4291 (2020).

[59] N. J. Cornish, T. B. Littenberg, B. Bécsy, K. Chatziioannou, J. A. Clark, S. Ghonge, and M. Millhouse, BayesWave analysis pipeline in the era of gravitational wave observations, Phys. Rev. D **103**, 044006 (2021).
[60] K. Nakamura, S. Horiuchi, M. Tanaka, K. Hayama, T. Takiwaki, and K. Kotake, Multimessenger signals of long-term core-collapse supernova simulations: Synergetic observation strategies, Mon. Not. R. Astron. Soc. **461**, 3296 (2016).
[61] S. Al Kharusi *et al.*, SNEWS 2.0: A next-generation supernova early warning system for multi-messenger astronomy, New J. Phys. **23**, 031201 (2021).
[62] M. Millhouse, N. J. Cornish, and T. Littenberg, Bayesian reconstruction of gravitational wave bursts using chirplets, Phys. Rev. D **97**, 104057 (2018).
[63] T. B. Littenberg and N. J. Cornish, Bayesian inference for spectral estimation of gravitational wave detector noise, Phys. Rev. D **91**, 084034 (2015).
[64] J. C. Brown, Calculation of a constant Q spectral transform, Acoust. Soc. Am. J. **89**, 425 (1991).
[65] J. B. Kanner, T. B. Littenberg, N. Cornish, M. Millhouse, E. Xhakaj, F. Salemi, M. Drago, G. Vedovato, and S. Klimenko, Leveraging waveform complexity for confident detection of gravitational waves, Phys. Rev. D **93**, 022002 (2016).
[66] Y. S. C. Lee, M. Millhouse, and A. Melatos, Enhancing the gravitational-wave burst detection confidence in expanded detector networks with the BayesWave pipeline, Phys. Rev. D **103**, 062002 (2021).
[67] M. M. Dolan, G. J. Mathews, D. D. Lam, N. Quynh Lan, G. J. Herczeg, and D. S. P. Dearborn, Evolutionary tracks for Betelgeuse, Astrophys. J. **819**, 7 (2016).
[68] F. Pannarale, R. Macas, and P. J. Sutton, Bayesian inference analysis of unmodelled gravitational-wave transients, Classical Quantum Gravity **36**, 035011 (2019).